Waves and Instabilities in Saturn's Magnetosheath: 1 Mirror Mode Waves and Their Impact on Magnetopause Reconnection

I. Cheng[1] , N. Achilleos[1] , X. Blanco-Cano[2], C. Bertucci[3] , N. Sergis[4] , C. Paranicas[5] , and P. Guio[6]

[1]Department of Physics and Astronomy, University College London, London, UK, [2]Instituto de Geofísica, Universidad Nacional Autónoma de México, Mexico, Mexico, [3]IAFE, UBA-CONICET, Buenos Aires, Argentina, [4]Hellenic Space Center, Athens, Greece, [5]Johns Hopkins University Applied Physics Laboratory, Laurel, MD, USA, [6]Department of Physics and Technology, Arctic University of Norway, Tromsø, Norway

Abstract A comprehensive catalog of 1,589 Saturn magnetosheath traversals by Cassini between 2004 and 2012 was used to perform a statistical study of mirror mode (MM) waves and assess their role in influencing magnetic reconnection at the magnetopause (MP). MM waves have been observed in many planetary magnetospheres and magnetosheaths, comets and the solar wind. Understanding the conditions under which they grow and dominate can reveal their role in influencing plasma dynamics. Using a thresholding method on both magnetic field and plasma data, MM wave candidates can be identified. The magnetic field characteristics and occurrence distributions of these waves against different locations and conditions were found. MM waves were found from 4 to 19 hr local time (partly due to data coverage), and distances of 0–12 R_S from the magnetopause (MP). The occurrence of MM dips was more frequent near the MP and magnetosheath flanks, analogous to the Jovian system. MM dips exhibited a minimum field strength saturation ∼0.5 nT, with the largest dip inferred to be in mirror-stable plasma. Notably, larger amplitude MM dips were typically found nearer the MP boundary which increases $\Delta\beta$ across the boundary thus increasing the magnetic shear necessary for the onset of MP reconnection. Thus, MM waves may be important in plasma dynamics near Saturn's magnetopause.

Plain Language Summary Mirror mode waves (MM waves) are fluctuations in plasma density and magnetic fields that move with the bulk flow. They are commonly observed by spacecraft around planetary magnetospheres and other space environments. Their growth occurs when the plasma temperature perpendicular-to-magnetic-field is greater than some threshold of the temperature parallel-to-magnetic-field direction. After reaching saturation, some MM structures can remain stable for a long time. These waves can transfer energy between particles and electromagnetic fields, and could also influence more energetic events like magnetic reconnection. This study investigates the nature and role of mirror mode waves in Saturn's magnetosheath and surroundings.

1. Introduction

The mirror instability is common in high plasma β environments like planetary and cometary magnetosheaths. It could be triggered by energy sources from fluid and kinetic plasma processes at the bow shock (BS), within the magnetosheath plasma, and at the magnetopause (MP). Understanding these plasma processes would contribute both to fundamental plasma physics, such as wave-particle interactions, and to a deeper understanding of the role of the magnetosheath as an interface between the solar wind and the planetary magnetosphere.

In a high plasma-β environment such as a planetary magnetosheath, the plasma motion dominates which may lead to more turbulence. For Saturn's magnetosheath, plasma β ranges from order 1 to order 100, with a typical value of ∼10 (Masters et al., 2012). Consequently, it is a region of high wave activity with fluctuations over a broad range of frequencies ∼10^{-4} to 1 Hz (Hadid et al., 2015). The plasma within exhibits conditions such as proton temperature anisotropies

$$a_p = T_\perp/T_\parallel, \tag{1}$$

coupled with high plasma-β created by compression and preferential perpendicular heating at quasi-perpendicular bow shock, and further compression that takes place as the plasma and fields pileup near the subsolar MP (Tsurutani et al., 1982). When a_p and β are sufficiently large, they can produce local conditions necessary to drive the growth of mirror instability.

Assuming a homogeneous plasma with a bi-Maxwellian single ion distribution and a cold electron component, the temperature anisotropy threshold for the mirror instability is (Hasegawa, 1969):

$$\frac{T_\perp}{T_\parallel} > 1 + \frac{1}{\beta_\perp}, \tag{2}$$

where T is the ion temperature, β is the plasma beta, $\perp$ and $\parallel$ indicate perpendicular-to- and parallel-to-magnetic-field directions. Interestingly, the mirror instability criteria are identical in both fluid-only and mixed kinetic-fluid treatments even though this is inherently a kinetic instability (Southwood & Kivelson, 1993). Equation 2 suggests that mirror unstable plasma occurs in conditions of high β and $T_\perp > T_\parallel$. Mechanisms that could lead to anisotropic temperature plasmas include pickup ions, quasi-perpendicular shock compression and heating, and magnetic field line draping at the MP leading to field compression. The field line draping could also produce a plasma depletion layer (PDL), thus a reduced plasma β, near the subsolar MP due to a "squeezing" force that pushes plasma out of the region of the strong magnetic field to maintain constant total pressure (Slavin et al., 1983).

Two kinetic wave modes have been reported to grow and dominate in the magnetosheath plasma due to the ion temperature anisotropy that pervades throughout. The ion-cyclotron (IC) mode and mirror mode (MM) instabilities are generated by $a_p > 1$ temperature anisotropies, and they dominate when the plasma β is low and high, respectively. At Earth, IC waves are typically found behind the weaker quasi-perpendicular bow shocks and in the PDL, whilst MM waves are usually located behind strong quasi-perpendicular bow shocks and in the middle magnetosheath (Hubert, 1994).

The terms drift-mirror (DM) and mirror mode (MM) refer to the same underlying instability. The DM mode (Hasegawa, 1969) results in a low-frequency plasma mode (below the ion gyrofrequency Ω_i), whilst the MM is a special case of DM in that they are purely growing compressional plasma modes with zero real frequency (i.e., non-oscillatory and non-propagating). However, the growth criterion for both instabilities is the same. The DM instability is caused by streaming ions along the magnetic field, shifting the real frequency to a non-zero value (Zhao et al., 2019). The DM mode is found to exist close to the subsolar MP (Schwartz et al., 1996). The identification of waves in Earth's magnetosheath by Denton et al. (1995) identified DM waves in the frequency range of 0.01–0.04 Hz. Hereafter, DM and MM will not be explicitly distinguished and the acronym MM will be used unless otherwise stated.

Although MM structures are non-propagating waves in the plasma rest frame as the real angular frequency $\omega_r \sim 0$ and thus phase velocity $v_p \sim 0$, they are spatially oscillating disturbances that can be advected along with the plasma flow. Purely spatially oscillating disturbances also have an associated wavevector $\vec{k} = \vec{k}_\perp + \vec{k}_\parallel$, the direction along which the disturbance oscillates with a spatial scale $\lambda = 2\pi/|\vec{k}|$. For the MM structure, $\vec{k}$ is usually at large angles to the background field $\vec{B_0}$ (i.e., $k_\perp \gg k_\parallel$). This indicates that oscillations of MM structures have parallel length scales much greater than perpendicular length scales $\left(\lambda_\parallel \gg \lambda_\perp\right)$, in line with the idea of MM waves as elongated "magnetic bottles." These waves tend to grow obliquely to the background magnetic field direction (Gary, 1992). That is, they represent a compressional disturbance in the magnetic field produced by perturbation field vector $\delta\vec{B} = \delta\vec{B_0}e^{i\vec{k}\cdot\vec{r}}$ whose dominant component $\delta\vec{B}_\parallel$ is parallel or anti-parallel to the background field $\vec{B_0}$. This type of $\delta\vec{B}$ thus produces strong and weak field regions, with small perpendicular perturbations $\delta\vec{B}_\perp$ that contribute to the bending of field lines as seen in Figure 1b. Thus, the MM waves may be described as linearly polarized waves as the perturbation field vector $\delta\vec{B}$ oscillates mostly in a single direction (in the x–z plane of Figure 1b). Note that DM waves may become elliptically polarized instead of linearly polarized due to the drift velocity of the waves (Génot et al., 2001).
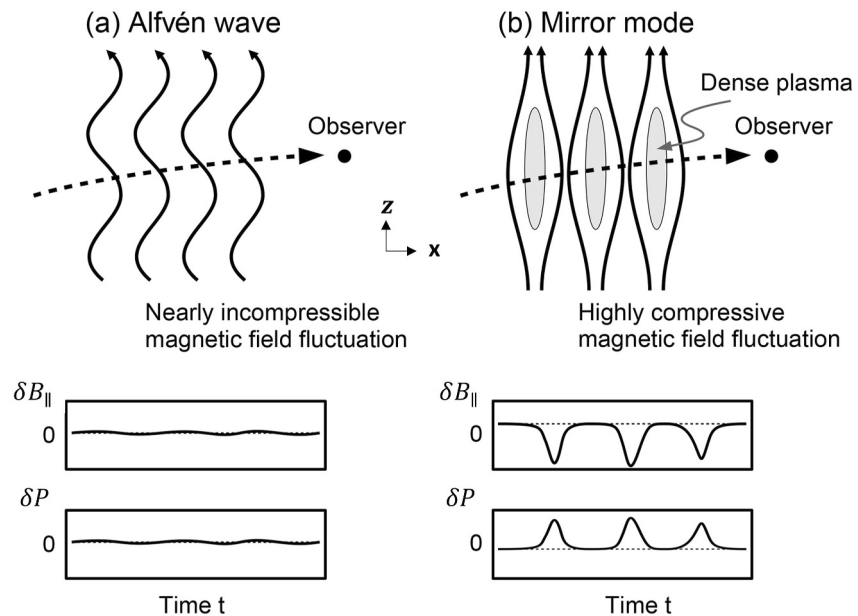
Figure 1. Schematic illustrating (a) Alfvenic/Ion cyclotron fluctuations and (b) mirror mode fluctuations. The corresponding bottom panels show the magnetic field and plasma pressure fluctuations of an arbitrary spacecraft trajectory (shown by the dashed line) through the structures. Modified from Schmid et al. (2020).

In comparison, an ion cyclotron (IC) wave is left-hand circularly polarized when propagating at 0° to $\overrightarrow{B_0}$ meaning that as the wave (truly) propagates along the background magnetic field in the plasma rest frame, the perturbation of the magnetic field direction rotates in the same sense as the local ion gyromotion, with small changes in the field magnitude, whilst the density fluctuations correlate positively with $\delta\mathbf{B}_\parallel$ (Hubert, 1994). Figure 1 compares the magnetic field structure of the two modes and shows the expected change in parallel magnetic field and plasma pressure for a spacecraft traversing these structures.

Observations of the MM in space plasmas have been carried out since the 1970s using Explorer 33 measurements (Crooker & Siscoe, 1977). Thereafter, observations of MM waves within Earth's magnetosheath, as far downstream as 200 R_E, have been reported by various authors (e.g., Hubert, 1994; Lacombe & Belmont, 1995; Tsurutani et al., 1982; Tsurutani et al., 1984). MM waves were found in Earth's inner magnetosphere (Soto-Chavez et al., 2019) and near the cusp as a result of magnetic reconnection (Nykyri et al., 2019). MM waves in other space environments have also been reported such as in Mars' magnetic pileup boundary (Bertucci et al., 2004); in Venus' and Mars' magnetosheath as observed by the Venus Express and MAVEN spacecraft respectively (Volwerk et al., 2022; Wedlund et al., 2023); in Jupiter's magnetosheath (e.g., André et al., 2002; Balogh et al., 1992; Erdős & Balogh, 1996; Joy et al., 2006; Tsurutani et al., 1993) and in the wake of its moon Io (Huddleston et al., 1999; Russell et al., 1998); in Saturn's magnetosheath (e.g., Cattaneo et al., 1998; Violante et al., 1995) and middle magnetosphere (Russell et al., 2006); in the Uranian environment (Russell et al., 1989); cometary environments (Russell et al., 1987); and the solar wind where small amplitude compressional waves can persist for hours (Enríquez-Rivera et al., 2013; Russell et al., 2008, 2009; Tsurutani et al., 1992). In more extreme cases, they have also been observed in the sheath regions of interplanetary coronal mass ejections (ICME) (Ala-Lahti et al., 2018).

There are practical applications of MM waves such as in-flight calibration of fluxgate magnetometers. Schmid et al. (2020) showed the mirror mode technique can yield accurate magnetometer offset estimates which are necessary to obtain reliable absolute values of the magnetic field strength from the relative fluxgate readings.

MM waves advected to the MP could impact magnetic reconnection due to increased asymmetry of plasma β between the two regions separated by the MP current sheet. The alternating high and low plasma β regions created by MM waves and the $T_\perp > T_\parallel$ plasma temperature anisotropies may lead to patchy and sporadic reconnection (Hau et al., 2020; Violante et al., 1995).
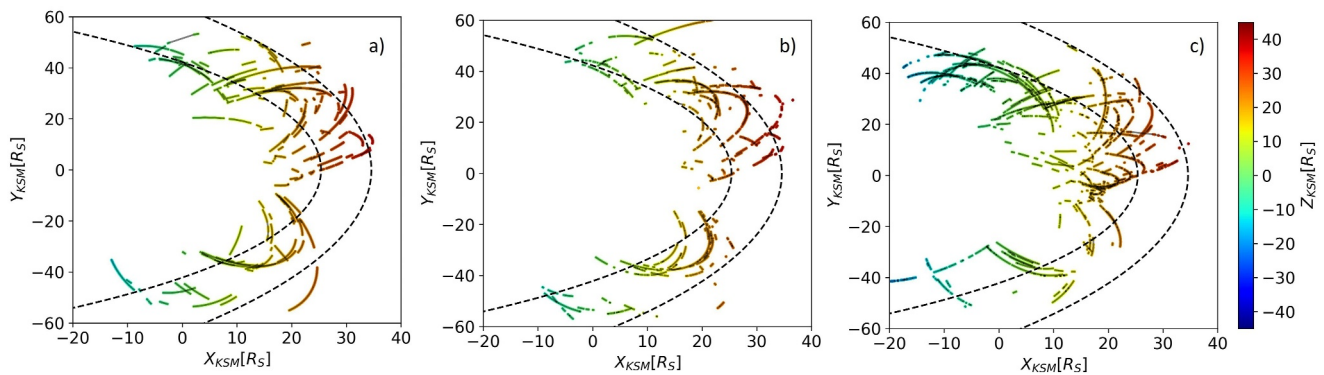
Figure 2. Magnetosheath traversals by Cassini between 27-06-2004 and 30-05-2012 projected onto the XY plane in Kronocentric Solar Magnetospheric (KSM) coordinates with determined plasma β, subject to availability of plasma data from CAPS and MIMI. The panels represent different magnetosheath traversal types: (a) BSI-MPI and MPO-BSO, (b) BSI-BSO, and (c) MPO-MPI. See main text for details. The color of the markers indicates Z coordinates in KSM. The dashed black curves give Saturn's bow shock and magnetopause nominal positions based on a dynamic pressure of 0.011 nPa. The BS and MP standoff distances are situated at 35 R_S and 25 R_S based on empirical models by Went et al. (2011) and Pilkington et al. (2015) respectively.

The goal of the present study is to answer the following questions regarding mirror mode waves (MMW) in Saturn's magnetosheath:

1. What are the characteristics and occurrence of MMW in Saturn's magnetosheath?
2. How do MMW impact the viability of magnetic reconnection at Saturn's magnetopause?

2. Cassini Data Set

For this study, magnetic field and plasma data were used to obtain the conditions in which the MMW were found. The following three instruments on board Cassini obtained the measurements: (a) The dual-technique magnetometer (MAG) (Dougherty et al., 2004). (b) The electron spectrometer (ELS) and the ion mass spectrometer (IMS) sensors of the Cassini Plasma Spectrometer (CAPS) instrument (Young et al., 2004). (c) The charge-energy-mass spectrometer (CHEMS) and the low energy magnetospheric measurements system (LEMMS) sensors of the Cassini magnetospheric imaging instrument (MIMI) (Krimigis et al., 2004).

MAG provides in situ magnetic field measurements. Both 1-s and 1-min averaged data were used in the Kronocentric solar magnetospheric (KSM) coordinate system, where X points from the center of Saturn to the Sun, Y points in the direction $\Omega \times X$ (where Ω is Saturn's rotational/magnetic dipole axis), and Z completes the right-handed coordinate system. Moments derived from averaged distributions in the ELS and IMS in situ data provide density and temperature measurements of electrons and ions. The ELS sensor has eight anodes which sweep through 63 logarithmic steps covering an energy range of 0.6 eV–28.25 keV in 2 s. The IMS sensor sweeps through 64 logarithmic steps every 4 s to cover an E/q range of 1–50 keV. Finally, MIMI provides in situ measurements of energetic particles. The CHEMS sensor detects energetic ions in the energy range of 2–220 keV/e, whilst the LEMMS sensor measures the energy range of ions between 0.03 and 18 MeV and electrons between 0.015 and 0.884 MeV.

The MAG, CAPS and MIMI data were obtained from The Planetary Plasma Interactions (PPI) Node of the Planetary Data System (PDS).

3. Methods

3.1. Extracting Magnetosheath Intervals

Magnetosheath traversals by Cassini were identified using the latest Saturn boundary crossing catalog (Cheng et al., 2022). The data set consists of 1,589 magnetosheath crossing intervals made by the Cassini spacecraft from 27 June 2004 to 29 May 2012, when plasma data from the CAPS instrument were broadly available. The median duration of a magnetosheath interval was 140 min with an interquratile range of 393 min. There are three types of magnetosheath traversals: BS ↔ MP, BSI → BSO and MPO → MPI. Figure 2 illustrates different kinds of magnetosheath traversals by Cassini.

Table 1
Counts of Magnetosheath Traversal Types Made by Cassini Between 27 June 2004 and 29 May 2012

SH traversal type	Count	Percentage (%)
BSI-MPI, MPO-BSO	182	11
BSI-BSO	409	26
MPO-MPI	998	63
	1,589	

The first type (BS ↔ MP) involves Cassini crossing consecutively both boundaries one after the other: a single inbound crossing of the BS and MP (BSI-MPI) or a single outbound crossing of the MP and BS boundaries (MPO-BSO). In this scenario, due to the lack of multiple crossings which usually indicate significant boundary dynamics, the boundaries were assumed to be moving smoothly between the first and second crossings. The second type (BSI → BSO) involves in-out crossings of the bow shock, and the third type (MPO → MPI) involves out-in crossings of the magnetopause twice. The counts of each type are summarized in Table 1. Saturn's magnetospheric boundaries are, more typically, quite dynamic as the majority of consecutive crossings are of the same boundary.

3.2. Calculating Pressures and Plasma β

The plasma β (ratio of plasma to magnetic pressure) is needed to evaluate the mirror instability criterion (Equation 2). The plasma pressure is determined by summing the contribution from each plasma species.

MAG data provide the magnetic field pressure, and moments derived from CAPS ELS data provide the thermal electron pressure (Lewis et al., 2008). The moments derived from CAPS IMS data provide the thermal ion pressures: H+, H_2^+/He^{2+} (species with mass-per-charge 2), W+ (water group ion species with mass-per-charge between 16 and 19) (Thomsen et al., 2010; Young et al., 2004). MIMI data (Krimigis et al., 2004) provide the energetic charged particle pressure (>10 keV electrons and ions). Unfortunately, due to the pointing constraint of the CAPS instrument, a vast majority of the thermal ion moments were unreliable (Thomsen et al., 2010). Thus, only some of our plasma beta calculations have full plasma β measurements which include thermal H^+ and H_2^+/He^{2+} pressures. Out of 1,589 magnetosheath intervals, only 28% had full plasma β measurements, while only 24% of individual data points had these measurements. This percentage is similar to the 70/387 (∼18%) of MP crossings with full plasma β on both sides of the MP current layer found by Masters et al. (2012). They also showed in a limited number of case studies that the pressure from energetic electrons and ions has a significant contribution to the total plasma pressure.

The magnetic pressure (in units of nPa) was computed using

$$P_B = \frac{B^2}{2\mu_0} \times 10^{-9}, \tag{3}$$

where B is the magnetic field strength in units of nT and $\mu_0 = 4\pi \times 10^{-7} \mathrm{Hm^{-1}}$ is the permeability of free space.

The thermal plasma pressure (in units of nPa) was computed using the gas equation

$$P_{th} = enT \times 10^9, \tag{4}$$

where n is the number density in units of $\mathrm{m^{-3}}$, T is the temperature in units of eV and $e = 1.6 \times 10^{-19}°\mathrm{C}$ is the electron charge for the conversion of energy T from eV to J.

The energetic particle pressure (in units of nPa) was computed using the formula found in Mauk et al. (2004):

$$P_{ener} = 4\pi(m/2)^{1/2}10^8\sum_i I_i\left(E_i \times 1.6 \times 10^{-9}\right)dE_i, \tag{5}$$

where E_i is the nominal energy for the ith energy channel in units of keV, m is the mass of the species in grams, dE_i is the bandwidth for the ith energy channel (in keV), and I_i is the particle intensity for the ith energy channel in units of $\mathrm{particles}/(\mathrm{cm^2\,s\,sr\,keV})$. The constant 1.6×10^{-9} converts keV to ergs. The 10^8 factor converts $\mathrm{dyne\,cm^{-2}}$ to nPa. Note that ideally, one wants the pressure in the plasma rest frame, but the pressure calculated from data is in the spacecraft rest frame, which would be an overestimate since the measured energy by MIMI is the particle thermal energy plus the bulk flow. However, for energetic protons of order 50 keV (Mauk et al., 2004), the thermal speed is ∼10^3 $\mathrm{km\,s^{-1}}$, which is 10× greater than the relative speed between the plasma

bulk flow and the spacecraft $\left(\sim 10^2 \text{ km s}^{-1}\right)$. Thus, the calculated pressure is expected to be overestimated by $\sim 0.2\%$ relative to the actual pressure.

There are limitations to the MIMI data set due to restricted pitch angle coverage. Thus, magnetic field-parallel and magnetic field-perpendicular temperatures are not calculated for these populations. It is worth noting that water group ions W+ (consisting of O^+, OH^+, H_2O^+, and H_3O^+ ions) typically exhibit sparse measurements in the magnetosheath, partly due to the large gyroradii that these ions experience. An O^+ ion with energy of 50 keV has a gyroradius larger than 2 R_S in a typical magnetosheath field of 1 nT, assuming 90° pitch angle where all energy is in the perpendicular motion. To overcome this sparse nature of the MIMI measurements, 5-min-averaged energetic particle measurements were used.

Another issue to account for is sunlight contamination of the instruments' sensors. Fortunately, the geometry of the MIMI instrument allows for determining the minimum angle between the sun-spacecraft line and the LEMMS LET boresight. To be conservative, a minimum angle of 60° was required for the particle measurements to be used in the determination of energetic particle pressure. The calculations of pressures and plasma β values were validated against Figure 1d in Masters et al. (2012). The uncertainty in the plasma β values could be estimated by statistical uncertainties due to the large number of samples obtained.

3.3. Mirror Mode Type Classification in Spacecraft Data

The approach in Joy et al. (2006) was used to identify and classify mirror modes in Saturn's magnetosheath. The method used statistics of the quartiles of the magnetic field to define a more suitable background field associated with three different types of mirror mode structures: "dips", "peaks" and "other" (quasi-periodic structures). The direction of the magnetic field perturbation relative to the background field remains a useful characteristic to distinguish between MM and IC waves in an anisotropic plasma (Krauss-Varban et al., 1994). A summary of the method is provided here for completeness.

The mirror mode detection criteria are as follows:

1. Field fluctuation $\delta B > 1$ nT, or relative fluctuation $\delta B / B > 0.133$ (which corresponds to a change in field pressure of 25%, given by $1 - (1 - \delta B / B)^2 = 0.25$).
2. Angle between maximum variance direction (obtained from minimum variance analysis) and the background field direction is <30° (Cattaneo et al., 1998; Joy et al., 2006), for the reason that most of the fluctuations are parallel to the background field.

If the above criteria are met, then the mirror modes are further classified into the following:

1. "Peak" if $a/b > 3$ and the background field is classified as "LQ"
2. "Dip" if $a/b < 1/3$ and the background field is classified as "UQ"
3. "Other" if $1/3 < a/b < 3$ and the background field is classified as "Median"

Where $a = \langle B - B_{UQ} \rangle$ and $b = \langle B_{LQ} - B \rangle$, are averaged over a 10-min window of 1-min strides, UQ and LQ are upper- and lower-quartiles respectively. A ratio $a/b > 1$ implies that on average, the field spikes above the UQ are more prominent than field spikes below the LQ, so the LQ field should be used as the background field. Conversely, a ratio $a/b < 1$ implies that on average, the field spikes below the LQ are more prominent than field spikes above the UQ, so the background field should be UQ. Negative values of a and b are not used for classification.

3.4. Shortest Distance to Nearest Boundary

The shortest distance between a spacecraft position and a magnetospheric boundary is given by a line which connects a point on the boundary to the spacecraft position, and the line must be normal to the boundary surface at this point. Two numerical methods were tested to solve this problem. Note that distances were only calculated for the BSMP-type magnetosheath traversal because it constrains the boundary positions and allows inference of upstream conditions, giving information on whether the magnetosphere was contracting or expanding.

In the BSMP magnetosheath traversal type, the first boundary crossing (e.g., BS) is used to infer the upstream dynamic pressure, and then infer the position of the other boundary (e.g., MP). On the second boundary crossing

(e.g., MP), the upstream dynamic pressure is inferred again to see how it has changed. This is again used to infer the position of the other boundary (e.g., BS). The dynamic pressure is interpolated between these two values to simulate a contracting or expanding magnetosphere. At each spacecraft position, a pair of magnetospheric boundaries (BS and MP) would be created based on the current upstream dynamic pressure value, from which the shortest distance to both boundaries could be determined using the numerical methods below.

The two numerical methods involved using (a) the BS and MP boundary normal vector (Pilkington et al., 2015) and (b) the Lagrange multiplier. In both cases, a system of four coupled non-linear equations was solved for the position on the MP surface which minimizes the distance between the spacecraft and the MP surface. For computing distances of all the BSMP-type magnetosheath intervals, the normal vector method was used. The implementation details can be found in Appendix A.

4. Results and Discussion

This section presents the results of the statistical analysis of MMW in 1,589 Saturn magnetosheath traversals observed by the Cassini spacecraft between the years 2004 and 2012. The summary statistics of different MM types are discussed followed by an analysis of their characteristics, occurrence distributions and amplitude variations with distance to the MP. Finally, we comment on their potential role in magnetic reconnection at the MP.

4.1. Overview of MM Waves

At Saturn, 71% of magnetosheath (SH) traversals contained at least one MM wave structure, compared to 61.5% at Jupiter (Joy et al., 2006). Of all the MM wave detections, 43.8% occurred in MPO-MPI traversals, 19.1% in BSI-BSO traversals, and 37.2% in BS-MP traversals. The counts for MM dips, peaks, and others were 1,794, 2,931 and 11,086 respectively. An MM wave was counted if consecutive data points of the same MM type were longer than 1 min in duration. The MM dips illustrated in Figure 3 have a duration of 2 min formed from 3 data points that satisfy the classification criteria. The percentage of MM wave types in the magnetosheath of Saturn, Jupiter and the Earth is summarized in Table 2.

4.2. A Case Study

This section uses a case study to show the classification results of the MM selection criteria described in the method Section 3.3.

Figure 3 shows the time interval between 30-07-2005 08:00:00 and 30-07-2005 13:00:00 where Cassini underwent an inbound BS crossing prior, followed by an inbound MP crossing (BSI-MPI). The magnetosphere was inferred to be expanding during this interval with a magnetopause standoff distance increasing from $\sim$18.0 R_S to $\sim$23.5 R_S, based on the method described in Section 3.4. The combination of magnetic and plasma pressures gives $\beta \sim 0.2$ in the magnetosphere and $\beta \sim 1$ in the magnetosheath for this crossing. The minimum and maximum standard deviation of the 5-min-averaged plasma β in this interval were 10^{-2} and 2 respectively, decreasing from high to low toward the MP.

Figure 4 shows the classification of mirror mode types in this magnetosheath interval. MM dips, shaded red in Figure 4a, were observed nearer to the MP, whilst sinusoidal fluctuations including some MM peaks were observed further away in the middle magnetosheath. For the dips, the magnetic field strength did not drop below around 1 nT as the spacecraft was approaching the MP. As Figures 3d and 3e show, the partial plasma β decreases whilst the minimum mirror criterion (i.e., the minimum temperature anisotropy needed) increases toward the MP boundary due to the presence of a PDL where the number density decreases significantly and magnetic field strength increases. Nonetheless, MM waves were observed within the PDL where the mirror criterion in the surrounding plasma was relatively high requiring a minimum anisotropy of $a_{min} > 20$ at times. In a high-β plasma regime, the general relationship linking the magnetic fluctuations $\delta B/B$ and number density fluctuations $\delta n/n$ in anisotropic plasma is given by Hasegawa (1969)

$$\frac{\delta n}{n} = \left(1 - \frac{T_\perp}{T_\parallel}\right)\frac{\delta B}{B}, \tag{6}$$
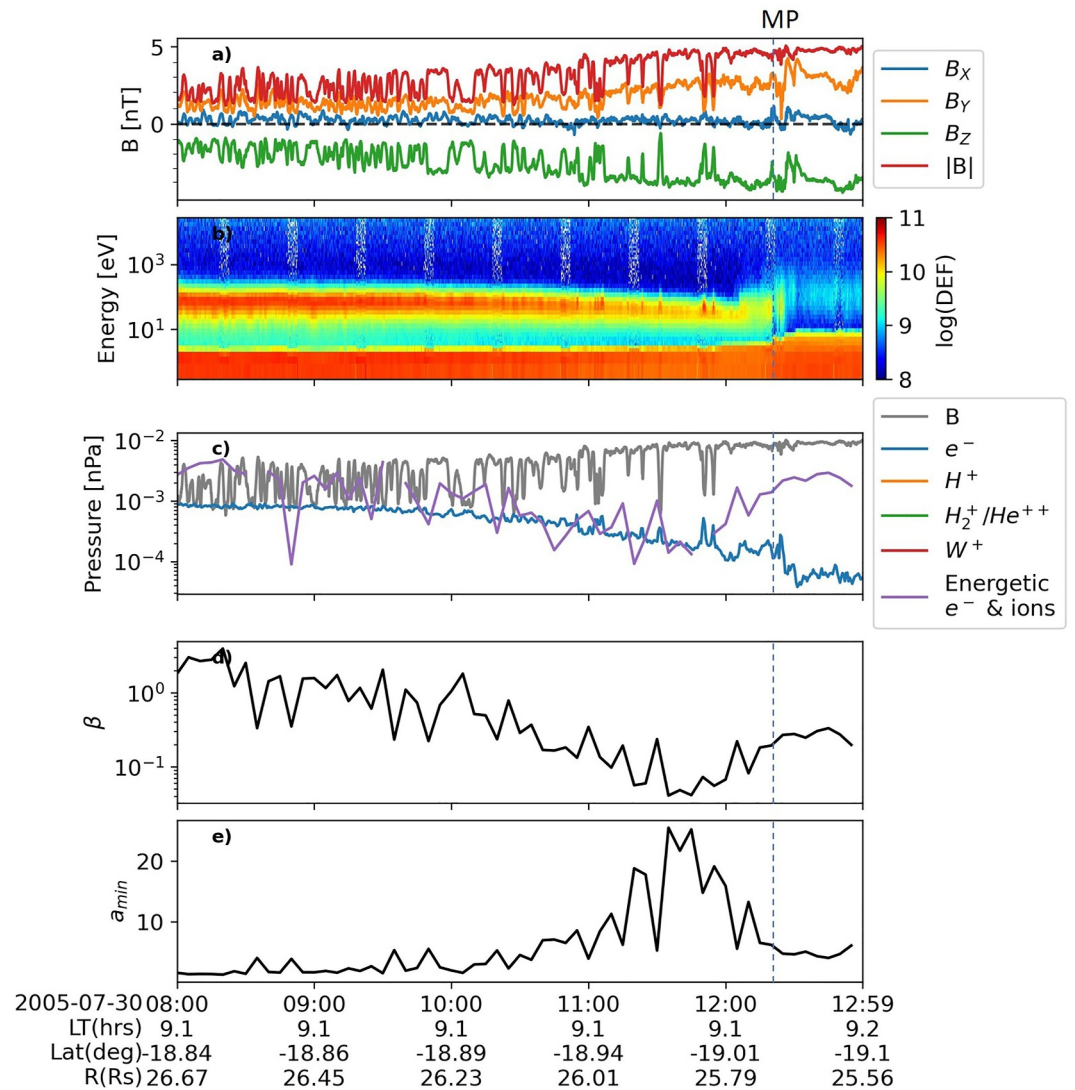
Figure 3. Exemplar magnetosheath traversal with evidence of mirror mode waves seen here as "dips" in the magnetic field magnitude. The panels are (a) Magnetic field in Kronocentric solar magnetospheric coordinates. (b) Energy-time spectrogram of electron Differential Energy Flux (DEF) $\left(\text{eV s}^{-1}\,\text{m}^{-2}\,\text{ster}^{-1}\,\text{eV}^{-1}\right)$ from ELS anode 5. The electrons below ≈ 10 eV are spacecraft photoelectrons. (c) Pressure (nPa) due to magnetic field and each charged particle population measured by Cassini CAPS and MIMI instruments (see Section 3.2). Some species are missing due to data gap in the CAPS/IMS sensor. (d) Partial plasma β, which could be partial or full depending on the availability of plasma data. (e) The minimum mirror criterion ($a_{\min} = 1 + 1/\beta$), assuming $\beta \approx \beta_\perp$. Ion temperature anisotropy $T_\perp/T_\parallel$ is required to be greater than this to make the mirror instability unstable. Finally, spacecraft ephemeris data are given below the x-axis of the plot.

where $T_\perp/T_\parallel$ is the ratio of perpendicular to parallel temperature relative to the direction of the background magnetic field. Equation 6 was used in Violante et al. (1995) to estimate the temperature anisotropy of plasma from Voyager data. For the current magnetosheath interval, anti-phase fluctuations between density and magnetic

Table 2
Percentage of MM Dips, Peaks, and Others in Different Planetary Magnetosheaths

| Magnetosheath environment	Dips (%)	Peaks (%)	Others (%)	Source
Saturn	11	19	70	This work
Jupiter	19	14	67	Joy et al. (2006)
Earth	40	19	42	Soucek et al. (2008)
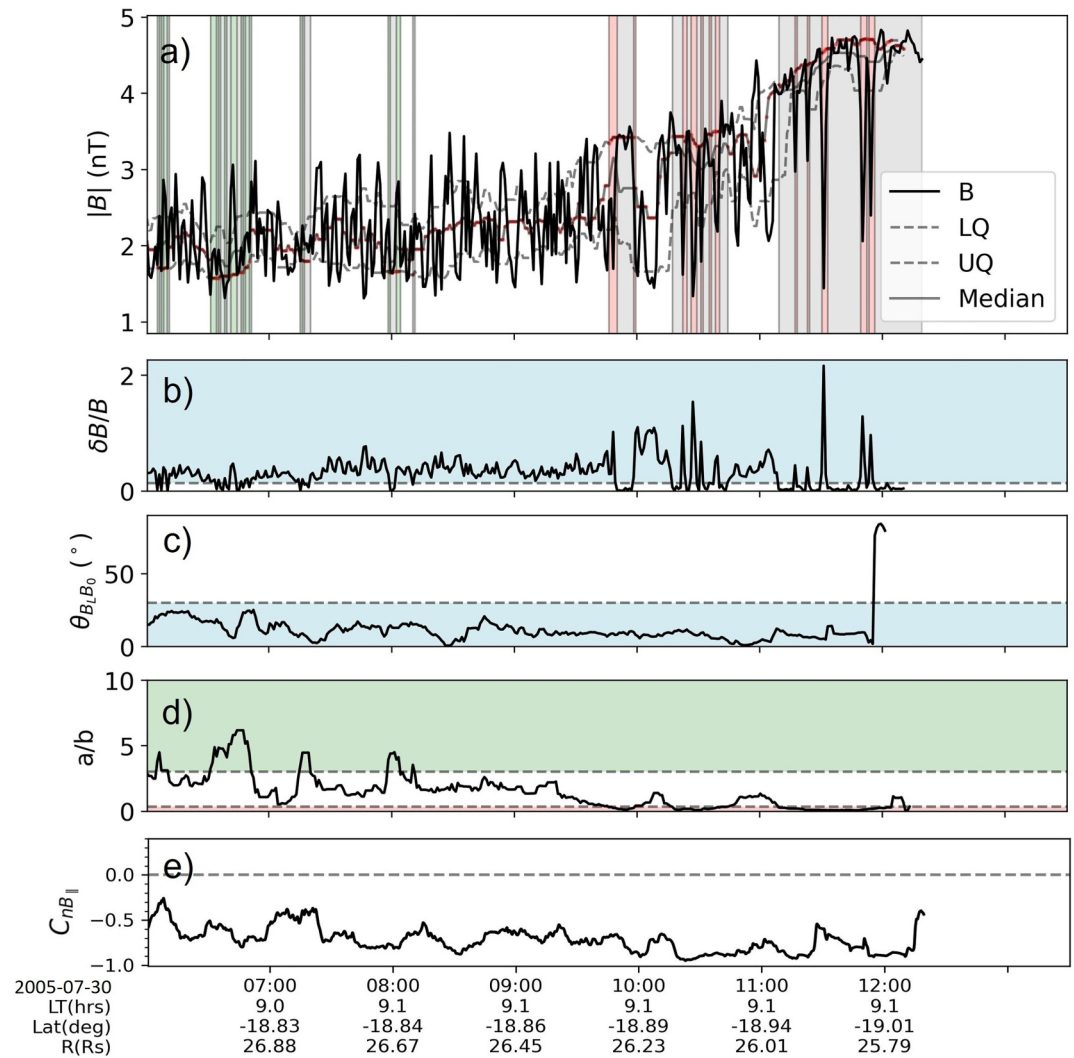
Figure 4. (a) Mirror mode case study identification and classification. The red, green, white, and gray shaded regions correspond to "dips", "peaks", "other", and "not mirror modes", respectively. (b, c) The criteria required (blue shaded regions) for mirror mode identification. (d) The criteria used to classify the type of mirror mode (color scheme same as panel a). (e) The parallel compressibility $C_{nB_\parallel}$.

field were observed implying $T_\perp/T_\parallel > 1$ (Equation 6). Using Equation 6 gives a median anisotropy of $T_\perp/T_\parallel = 1.82$ for the plasma between 11:00 and 12:00, which was less than the minimum anisotropy required for the plasma to be mirror unstable (Equation 2). This implies that the observed waves in the PDL were likely due to mirror modes advected by the plasma flow from the upstream region.

4.3. Saturn's Magnetosheath Conditions

Below is a summary of the magnetosheath conditions in which MMW were detected. Figure 5 shows the distributions of the magnetic field strength, plasma density and temperature of different species, plasma and magnetic pressures, plasma β and average flow speeds, as revealed by Cassini data. The pressure distributions show that the total plasma pressure is generally higher than the magnetic pressure. The peaks occur at similar pressures as in Figure 1e of Sulaiman et al. (2017), although their study considered the thermal plasma population only (<45 keV, MIMI instrument). The plasma β distribution shows a peak at around 10 but can vary by orders of magnitude typically from 1 to 100 (Krimigis et al., 2004; Sergis et al., 2013). The weaker upstream magnetic field at Saturn produces a higher plasma β and Alfvén Mach number than at the Earth (Sulaiman et al., 2016). Figures 5b and 5c show that the total density distribution has a single peak whilst the total temperature distribution
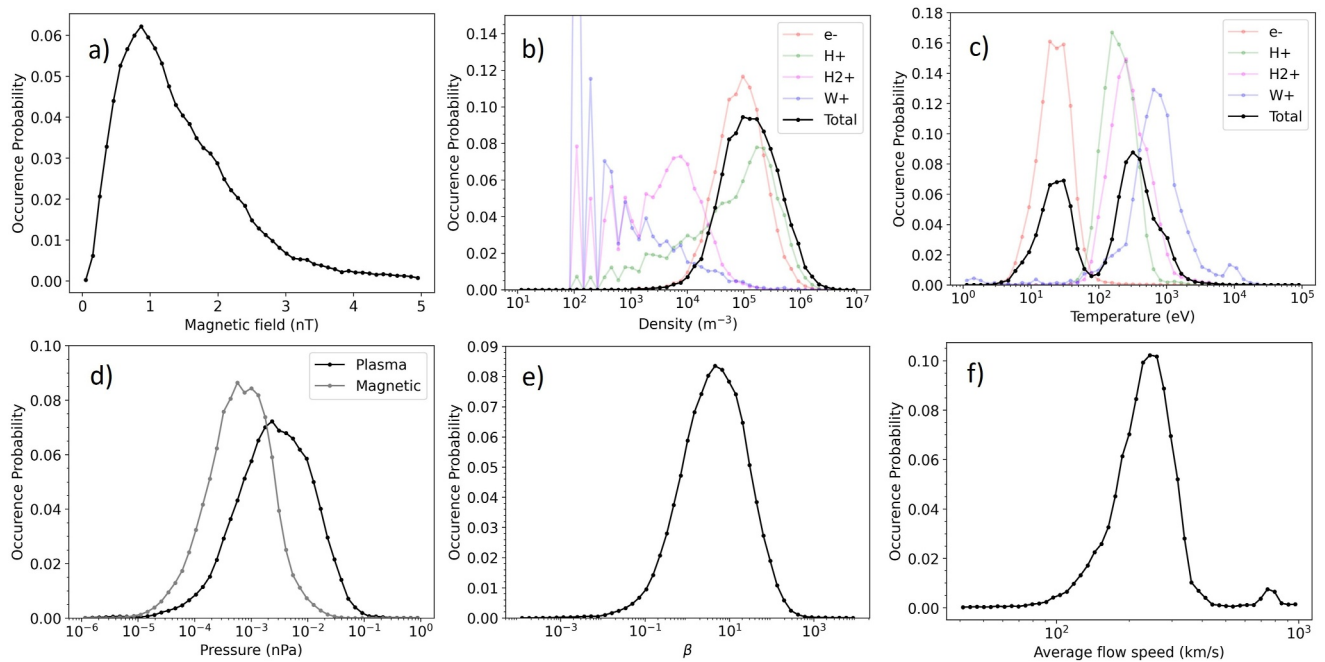
Figure 5. Distributions of (a) Magnetic field strength, (b) plasma number density for the thermal ions and electrons (the total is defined as the sum of each species present at the time of measurement), (c) plasma temperature for thermal ions and electrons, (d) plasma and magnetic pressure, (e) plasma β, (f) average magnetosheath flow speeds using CAPS/IMS measurements, based on 1,589 magnetosheath intervals.

has bi-modality with electron temperature peaking an order of magnitude lower than that of ions ($T_e \approx 0.1 T_p$). Figure 5f shows average plasma flow speeds in the magnetosheath from the CAPS/IMS sensor. This analysis revealed that 59% of all velocity measurements had a "not bad" quality flag, meaning that the spacecraft was not rolling and/or CAPS was actuating normally. The median speed was 226 km s^{-1}, with a lower quartile value of 178 km s^{-1} and an upper quartile value of 272 km s^{-1}. Ions were used to determine the bulk flow speed because the thermal kinetic energy of electrons could often be 100 times greater than the bulk flow kinetic energy (Arridge et al., 2009).

4.4. Occurrence of Mirror Mode Waves (MMW)

4.4.1. Boundary Distance Dependence

Figure 6 shows the dependence of MM type on MP distance. Data were collected into 1 R$_S$ bins relative to the nearest MP crossing and normalized by the total number of observations within each bin. MM waves were detected across large distances from 0 to 12 R$_S$ from the MP, implying a potential origin near the upstream quasi-perpendicular bow shock where the plasma becomes anisotropic due to preferential perpendicular heating. The top panel shows that the fraction of dips increases as the distance to the MP decreases. The second panel shows that the occurrence of peaks also increases with distance from the boundaries, peaking at ~ 5 R$_S$ from the BS, and 2–3 R$_S$ from the MP, after which its occurrence decreased. This suggests that the plasma remains mirror unstable for some distance after crossing the BS. A key distinction for dips was that their occurrence continued to increase up to the MP. These results were consistent with the case study in Section 4.2. The third panel shows that the fraction of other quasi-periodic structures falls as the distance from the MP increases.

The maximum occurrence of peaks relative to the MP was consistent with observations at Earth by the Cluster spacecraft where an abrupt transition of mirror structures from peaks to dips was found at ~ 2 R$_E$ from the MP (Soucek et al., 2008), and that peaks occur most frequently in the central magnetosheath whilst dips occur most frequently close to the magnetopause (Soucek et al., 2015). Similar observations were found at Jupiter by Joy et al. (2006) although it was for time to the nearest boundary (Figure 6 left).
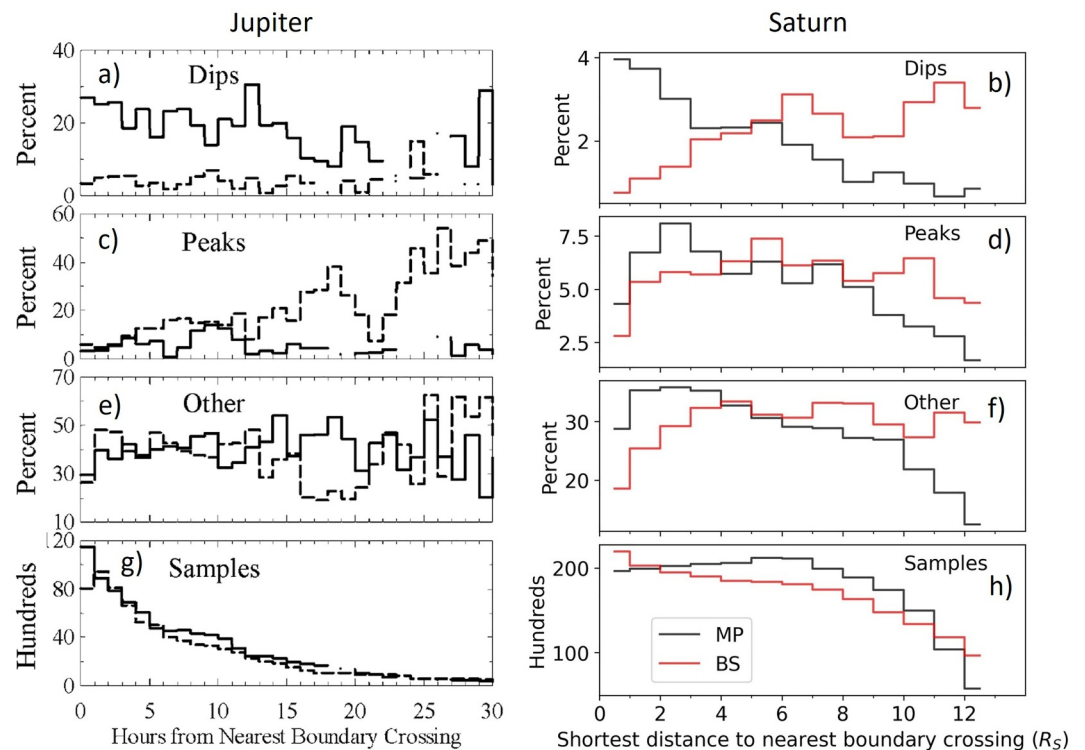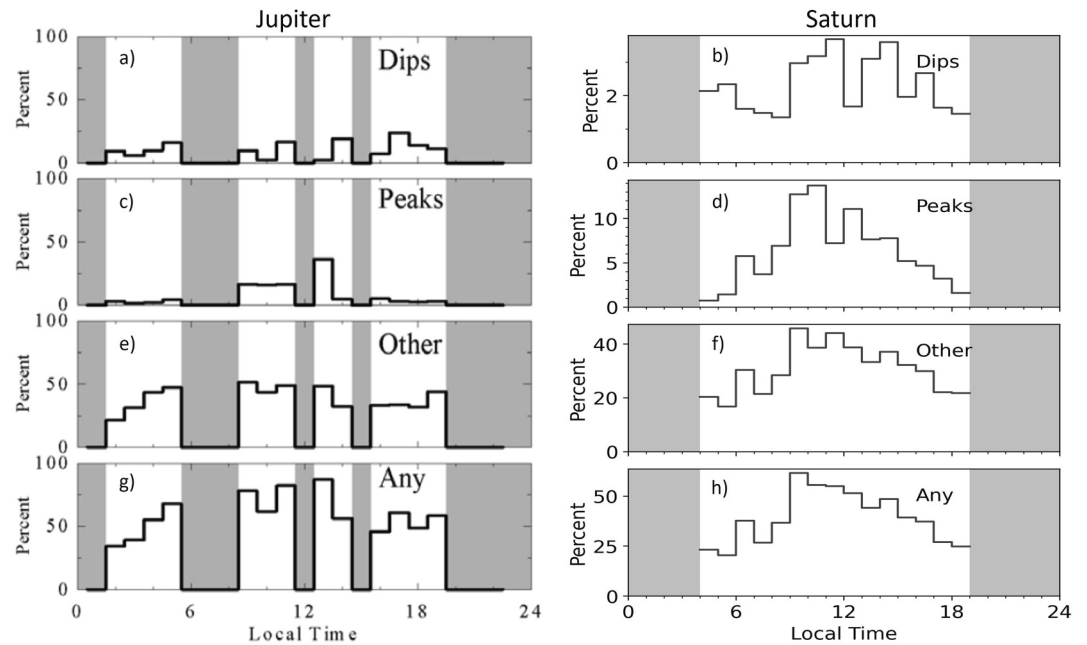
Figure 6. Occurrence distribution of dips (a, b), peaks (c, d), and other (e, f) mirror structures in Saturn's magnetosheath against distance to the nearest MP (solid, black) or BS (dashed, red) boundary. The bottom panels (g, h) show the number of observations (in hundreds) in each bin. The left column is for Jupiter taken from Joy et al. (2006). The right column is for Saturn.

4.4.2. Local Time Dependence

Figure 7 shows the dependence of MM type on local time. Data were collected into 1-hr local time bins and normalized by the total number of observations within each bin. Mirror structures, especially the "other" MM type, are most frequently observed near the subsolar point and gradually diminish in occurrence as the local time departs from noon at both Jupiter and Saturn. At both planets, peaks are more commonly observed near local noon and decrease toward flanks, although more gradually at Saturn than at Jupiter. For Saturn, dips comprised a larger fraction at the dawn flank compared to peaks. The local times with higher occurrences of dips include 4–7, 9–12 and 13–18 hr local time. For Jupiter, dips comprised a larger fraction at both flanks compared to peaks. At Earth, mirror mode dips were also frequently observed in the magnetosheath flanks (Soucek et al., 2008, 2015).

4.4.3. Magnetic Field Dependence

Figure 8 shows the MM type dependence on the local background magnetic field strength. Dips are more commonly observed in stronger background fields in comparison to peaks at both Jupiter (~2.5 nT) and Saturn (~1.3 nT), with correspondingly lower plasma β. At Saturn, the small event cluster at 0.5 nT could be associated with the field minima saturation within dips which could be quite variable (e.g., the red shaded regions in Figure 4a). In comparison, the field dips saturate at ~1.3 nT at Jupiter (Erdős & Balogh, 1996), but can be variable as seen with small event clusters near 0.5 and 1.0 nT (Joy et al., 2006). Peaks are typically observed in a weaker background field strength at both Jupiter (~1.4 nT) and Saturn (~0.5 nT), with correspondingly higher plasma β. The peak of the field strength distribution occurs at around 2.3 nT for Jupiter and around 1–2 nT for Saturn. "Other" quasi-sinusoidal mirror structures ranged from 1.6 to 2.3 nT for Jupiter and 0.5–1.0 nT for Saturn, with little clustering. The systematically lower field strength at Saturn is very likely due to the weaker IMF at Saturn, located at ~9 AU from the Sun, compared to Jupiter at ~5 AU.

Figure 7. Occurrence distribution of dips (a, b), peaks (c, d), other (e. f) and any (g, h) mirror structures versus local time. Shading indicates regions of no data coverage. Values indicate the percentage of the observations within each bin containing one type of MM wave. The left column is for Jupiter taken from Joy et al. (2006). The right column is for Saturn.

4.4.4. Plasma Beta Dependence

Figure 9 shows the dependence of MM type on plasma β, which was collected into bins of size 0.5 and the occurrence of each type of mirror mode structure was normalized by the total number of observations within each bin. There appears to be a dependence of mirror mode types on plasma β: low β plasma ($\sim \beta < 4$ for Saturn and $\sim \beta < 3$ for Jupiter) is usually populated by dips, while peaks are observed over a wide range of β from 4 to over 20 for Saturn and from 3 to 7 for Jupiter.
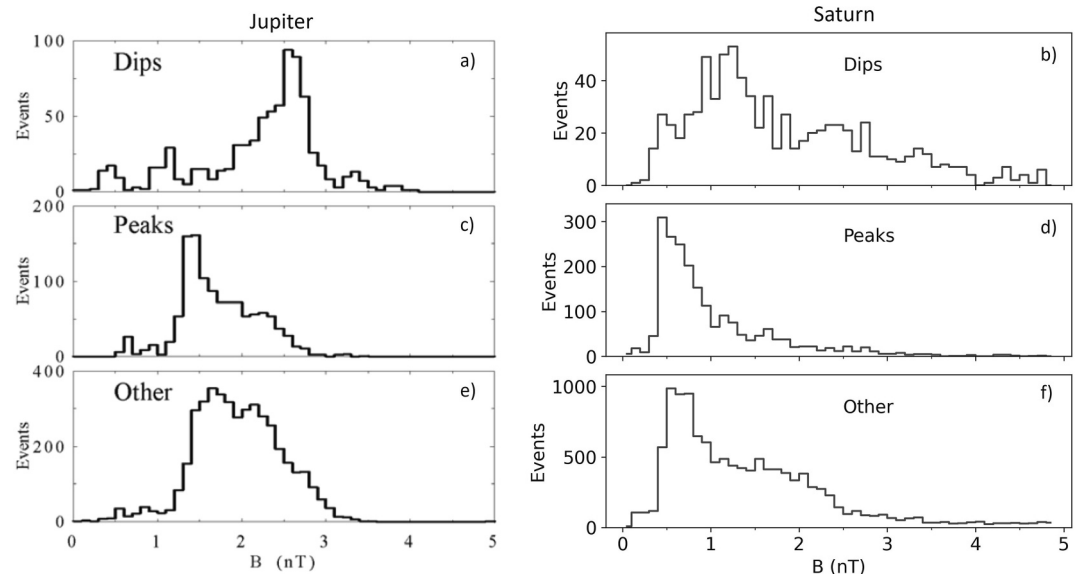
Figure 8. Distribution of B (nT) in 0.1 nT bins for dips (a, b), peaks (c, d) and other (e, f) mirror structures. The left column is for Jupiter taken from Joy et al. (2006). The right column is for Saturn.
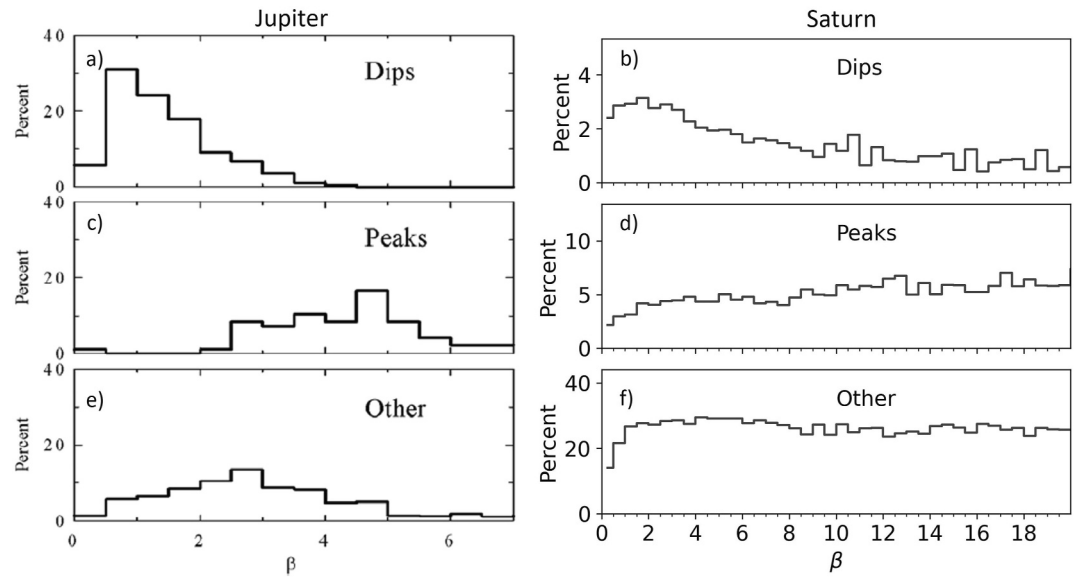
Figure 9. Occurrence distribution of dips (a, b), peaks (c, d) and other (e, f) mirror structures versus plasma β in bins of size 0.5. The left plot is for Jupiter taken from Joy et al. (2006). The right plot is for Saturn.

For fixed density and temperature, lower β implies higher magnetic field strength which is consistent with the distribution for dips shown in Figure 8. "Other" mirror structures are observed over a wider range of β values, with no preference for any particular value at Saturn, but appear to peak at around 3 at Jupiter.

4.4.5. Temperature Anisotropy

Figure 10a shows the distributions of temperature anisotropy for MM dips and peaks. The anisotropy values were estimated using Equation 6. For dips, the median value of $T_\perp/T_\parallel$ was 0.935 ± 0.033. For peaks, the median value of $T_\perp/T_\parallel$ was 1.075 ± 0.019. A Kolmogorov-Smirnov (KS) test between the two distributions was performed. If the KS statistic was small or the p-value was high compared to the significance level $\alpha = 0.1$, the null hypothesis that the two samples came from the same distribution is not rejected. The obtained p-value was $10^{-15} < \alpha$. Thus, the null hypothesis is rejected implying that the temperature anisotropy values for peaks and dips come from different underlying distributions. Note that Equation 6 assumes a homogeneous plasma with a single bi-Maxwellian ion distribution and cold electron component. In reality, Saturn's plasma is inhomogeneous and has multiple components of ions. Furthermore, Equation 6 also requires high plasma β. Therefore, this equation estimates the plasma anisotropy in the limit these conditions hold.

Figure 10b shows that 46% of 500 largest MM peaks and 83% of 500 largest MM dips in the data set were found to occur in the mirror unstable and mirror stable region in the temperature anisotropy-β parameter space, respectively. The lower percentage of peaks in the unstable region could be due to the inherently more difficult detection
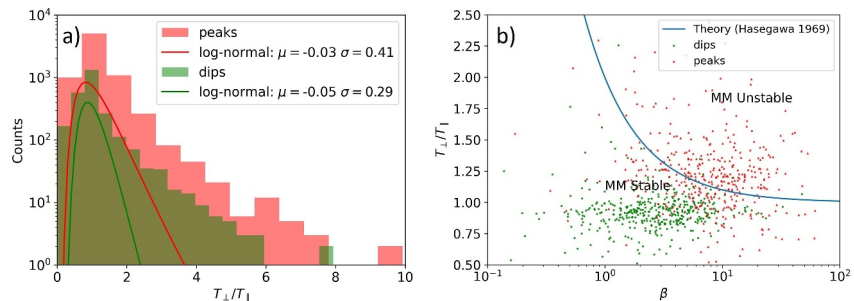
Figure 10. (a) Distributions of MM peaks and dips versus anisotropy. (b) Anisotropy-β plane illustrating the locations of 500 MM dips and 500 MM peaks with the largest-amplitude in this parameter space.
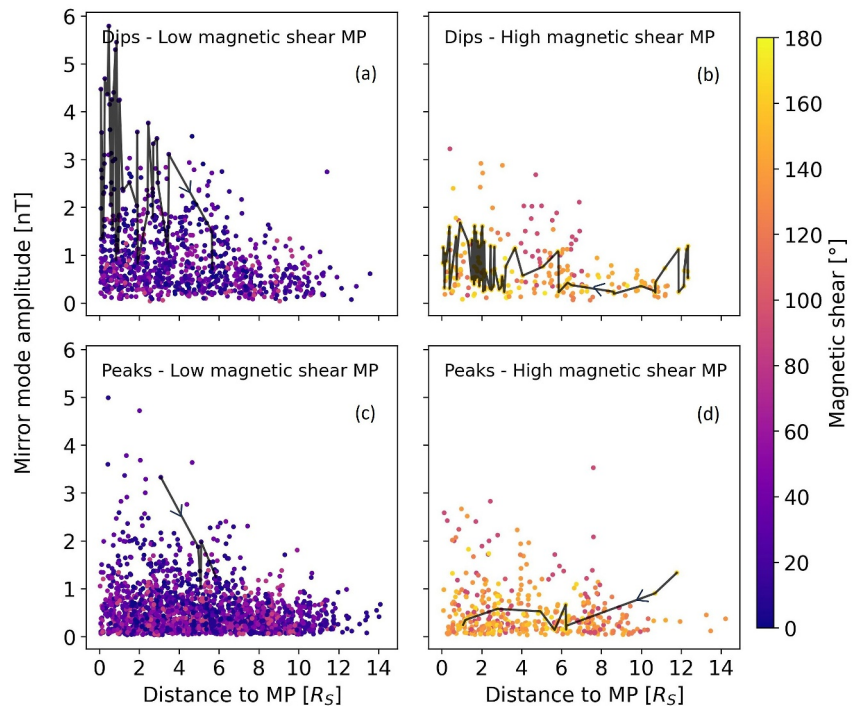
Figure 11. A scatter plot of the amplitude of mirror mode dips (a, b) and peaks (c, d) against the distance to MP with the magnetic shear of the MP shown by the color. The black lines show the observed mirror mode dips and peaks amplitudes along a single BSMP-type magnetosheath traversal characterized by the magnetic shear measurement at the MP crossing.

of peaks using the current detection methodology thus the false positive rate may be higher. Another reason is using Equation 6 to estimate the anisotropy instead of being directly measured. The observation of large dips in locally mirror-stable regions suggests that the spacecraft trajectory encountered these large amplitude dips after they had been advected to a locally stable region from their (presumably locally unstable) point of origin. Large amplitude dips may thus represent a late stage in the temporal evolution of the MM structures.

4.5. The Impact of Mirror Mode Waves on Magnetopause Reconnection

Plasma β conditions are important for magnetic reconnection at the MP as they could influence the range of magnetic shear angles across the MP at which reconnection is viable (Masters et al., 2012; Swisdak et al., 2003, 2010).

The following analysis was applied to the BSMP-type magnetosheath traversals as they had a more reliable and accurate determination of distances from the MP. For the current data set of BSMP-type magnetosheath traversals, the magnetic shear angles of the corresponding MP crossing ranged from 0.304° to 172°. The lower quartile, median and upper quartile were 18°, 39° and 82° respectively, with a mean error of ~5° based on magnetic field fluctuations on either side of the observed MP crossing. Violante et al. (1995) found that for a high magnetic shear MP, MM waves appear with increasing amplitude and decreasing frequency toward the MP, whilst for a low magnetic shear MP, MM waves appear in the PDL with smaller amplitudes and not growing. The results from the current study contradicted this to an extent. Figure 11 shows a plot of mirror mode wave amplitudes against distance to the MP under different magnetic shears. For the low magnetic shear panels ($<=90°$), the lines in the upper and lower panels show the successive dips and peaks detected along the magnetosheath traversal from 22-02-2012 17:31:00 to 23-02-2012 16:06:00 respectively. Similarly, for the high magnetic shear panels ($>90°$), the lines in the upper and lower panels show the successive dips and peaks detected along the magnetosheath traversal from 10-02-2012 20:24:00 to 16-02-2012 18:11:00 respectively. This plot illustrates the following two points:

1. For high magnetic shear MP ($>90°$), the amplitude of MM waves did not seem to increase as significantly as it did for low magnetic shear angles as they approached the MP.

2. For low magnetic shear MP ($\leq 90°$), the amplitude of MM waves tended to grow toward the MP, especially for dips, although not always the case as seen in the range of scatter.

In addition, Figure 11 shows that there are 18 dips and 6 peaks in the low magnetic shear MP with an amplitude larger than the maximum amplitude in the corresponding high magnetic shear MP. The more frequent high-amplitude events for low magnetic shear MP suggest that the magnetic shear angle which impacts reconnection efficiency may also impact the growth of MM waves. This could also be due to the compression of the background magnetic field as it piles up in front of the MP leading to a larger amplitude of the existing MM wave. For a low magnetic shear MP, reconnection may likely be suppressed due to diamagnetic effects. This could produce a more efficient pile-up of magnetic flux in front of the MP increasing the magnetic field and reducing the local plasma density. This draping of magnetic flux could increase the temperature anisotropy of the plasma (due to higher gyrofrequency from a stronger field) and increase growth rates. Indeed, as plasma beta drops due to the pileup of magnetic flux, the linear growth rate tends to decrease as shown in the companion paper (Cheng et al., 2024). It is a competing factor with temperature anisotropy. However, pressure from the presence of ions near the MP (Liou et al., 2021) could also increase the plasma beta. Furthermore, given the proximity to the MP, the non-linear growth phase of MMW is expected to have begun, thus the sensitivity of the growth rate on these factors is likely altered. Therefore, the impact of this combination of factors on the growth rate remains uncertain. As seen in Figure 11, despite some occurrences of larger amplitude MM waves closer to a lower magnetic shear MP, many small amplitude MM waves under low magnetic shear MP conditions are also observed, consistent with previous observations by Violante et al. (1995).

The change in plasma β across the MP increases significantly in the presence of large amplitude, adjacent MM dips, as the local magnetic field becomes weaker and plasma density becomes higher leading to higher plasma β in the local magnetosheath. The fact that MM wave amplitude variations tend to be larger for lower magnetic shear MP (Figure 11) suggest that they have an important role in affecting the viability of magnetic reconnection at low magnetic shear MP and in local time sectors near to local noon. As MM dips were found more frequently close to the MP (Figure 6), this would lead to greater $\Delta\beta$ across the MP, causing the onset of magnetic reconnection to be restricted to near anti-parallel magnetic fields between magnetoheath and magnetosphere (Swisdak et al., 2003). All estimates of magnetic shear are based on the general diamagnetic suppression condition given by Swisdak et al. (2010)

$$|\Delta\beta| > \frac{2L}{d_i}\tan\left(\frac{\theta}{2}\right), \tag{7}$$

where L is the current layer thickness, d_i is the ion inertial length and θ is the magnetic shear angle across the current layer. Essentially, the theory suggests that a higher $|\Delta\beta|$ across the current layer is less favorable for reconnection as the associated diamagnetic drift of charged particles can disrupt the reconnection jets.

The following scenarios are based on MM waves found in this study. Of the 69% of BSMP-type SH traversals (125/182) with at least one or more dips and peaks identified, the biggest dip had an amplitude of -6.2 nT and was at 0.28 R_s from the MP. For this event, the partial $\Delta\beta$ across the MP could increase from ~1 to over 20, restricting reconnection to magnetic shear angles $\geq 155°$; close to anti-parallel (Figure 12). The prior values of $\Delta\beta$ were obtained by taking the ambient pressures near the MP outside of the MMW influence. Considering the 25% of dips closest to the MP, the lower quartile amplitude of dips was ~ -1.5 nT. Assuming a background magnetosheath field of 4 nT and plasma pressure of $\sim 10^{-2}$ nPa, and a magnetospheric plasma β of 0.2, such a dip would produce a corresponding $\Delta\beta \sim 7$ compared to $\Delta\beta \sim 3$ without the dip, limiting the possibility of reconnection to magnetic shear angles $\geq 120°$.

The biggest peak had an amplitude of $+5$ nT and was at 0.45 R_S from the MP. Considering the 25% of peaks closest to the MP, the upper quartile amplitude of peaks was $\sim +0.9$ nT. Since an increase in magnetic field strength and a decrease in plasma density leads to reduced plasma beta, they will generally lead to a smaller $\Delta\beta$ at the MP, thus relaxing the magnetic shear necessary for reconnection to be possible. Both types of MM waves alter the conditions necessary for magnetic reconnection at the MP. However, dips are expected to play a bigger role as they increase in occurrence up to the MP, whereas peaks subside (Figure 6).
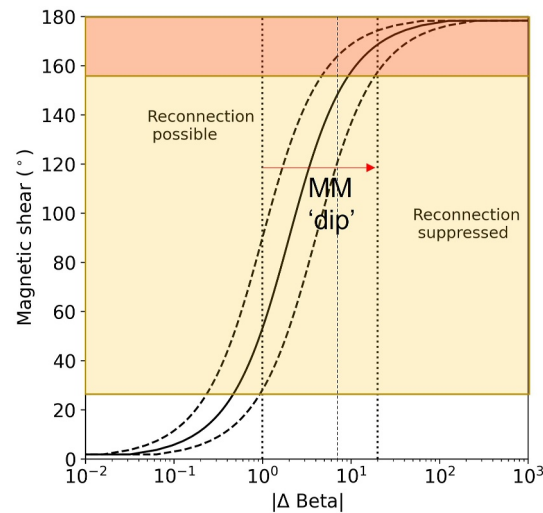
Figure 12. Diamagnetic suppression of magnetic reconnection in the magnetic shear-$\Delta\beta$ parameter space. The curves are calculated using Equation 7, where the solid line corresponds to a current sheet thickness $L = d_i$, and the dashed lines on the left and right of it correspond to $L = 0.5\ d_i$ and $L = 2\ d_i$, respectively. The light orange region indicates the range of magnetic shear angles where reconnection is possible without an MM dip, and the dark orange region is the analogous range in the presence of a large amplitude MM dip.

A significant increase in the asymmetry of plasma β between two sides of a reconnecting current sheet due to MM waves has also been found at the Earth using MMS data (Zhong et al., 2022). In addition, although a single MMW could exist in isolation (Winterhalter et al., 1994; Zhang et al., 2008), most MM waves in planetary magnetosheath occur in a series, so-called MM trains (Tsurutani et al., 2011). This could mean that magnetic reconnection would be repeatedly restricted to almost anti-parallel magnetic field shear configurations, making reconnection sporadic or patchy (Tsurutani et al., 1982). Cheng et al. (2021) found that electron heating events at Saturn's MP were typically found in the "reconnection possible" regime, further demonstrating the influence of MM waves on particle energization at the MP.

The amplitude and occurrence of MM in Saturn's magnetosheath were consistent with other planetary magnetosheaths where their occurrence rate was highest in the central or inner magnetosheath (e.g., Soucek et al., 2015), but was opposite to that found in ICME sheath regions where the amplitude and occurrence rate of MM was the largest closer to the shock (Ala-Lahti et al., 2018). The difference in growth is likely due to a smaller temperature anisotropy and the lack of magnetic field line draping providing another source of free energy in the ICME sheath.

Extreme space weather at Saturn (Burne et al., 2023) could produce even stronger shocks leading to more anisotropic plasma and faster growth rates for MM waves. This may lead to even larger amplitude MM waves forming in the magnetosheath that could impact the local structure of the magnetopause.

5. Conclusions

A statistical analysis of mirror mode (MM) waves in Saturn's magnetosheath was performed using magnetic field and plasma data from Cassini, characterizing their occurrence distribution against different locations and conditions. Finally, the impact of MMW on magnetopause reconnection was discussed. The main findings are summarized below:

1. **Occurrence:** The occurrence of different MM types is influenced by the proximity of their observed location to the MP and BS boundaries as well as local time. MM waves were found from 4 to 19 hr local time, and distances 0–$12\,R_S$ from the MP. MM dips occurred more frequently close to the MP and along the flanks of the magnetosheath (as is the case for the Jovian system),
2. **Characteristics:** MM dips exhibited a minimum field strength of ~0.5 nT. 83% of dips were in mirror stable region, whilst 46% peaks were in mirror unstable region.
3. **Boundary effects:** Larger amplitude MM dips tend to be found closer to the MP boundary suggesting that the plasma may remain mirror-unstable as it convects from the BS toward the MP, allowing growth for a long

duration. Near the magnetopause, large amplitude MM dips may restrict magnetopause reconnection to near anti-parallel magnetic shear due to increased $\Delta\beta$ which causes diamagnetic suppression.

This work led to a new question: Which mode dominates in Saturn's magnetosheath, ion cyclotron (IC) waves or MMW? Answering this question would require the identification of IC waves using magnetic spectrograms in Saturn's magnetosheath. The IC waves could be identified using such data to look for signatures of intense power spectral density at frequencies below the local proton and water ion gyrofrequencies (Meeks & Simon, 2017). 3D hybrid simulations of MM waves could shed new light on the non-linear processes involved and perform spatial-temporal analysis on how they modulate reconnection at the magnetopause. Ultimately, these kinds of numerical studies would further our understanding of the role of MM waves in coupling the energy from the solar wind to the planetary magnetosphere.

Appendix A: The Minimum Distance to a Boundary Surface

The shortest distance between a point $P = (x_p, y_p, z_p)$ and a surface S is the normal vector $\vec{n}$ on the surface that passes through P.

For the magnetopause boundary, the radial distance of the model surface r_{MP} is given by Arridge et al. (2006)

$$r_{MP}(x, y, z, K) = r_0\left(\frac{2}{1 + x/r}\right)^K \tag{A1}$$

where r_0 is the MP subsolar standoff distance, the exponent K is the flaring parameter that controls whether the magnetopause is open or closed, x, y, z are the KSM coordinates of a point on the MP surface and $r = \left(x^2 + y^2 + z^2\right)^{\frac{1}{2}}$ is the radial distance to that point.

The normal vector of the model surface is given by setting the derivative of $r_0(x, y, z, K)$ to 0. The normal vector for the MP surface is given by:

$$
\begin{aligned}
n_x &= \left(\frac{2}{1 + x/r}\right)^{-K} \frac{x - Kx + Kr}{r} \\
n_y &= y\left(\frac{2}{1 + x/r}\right)^{-K} \frac{x - Kx + Kr}{r(x + r)} \\
n_z &= z\left(\frac{2}{1 + x/r}\right)^{-K} \frac{x - Kx + Kr}{r(x + r)}
\end{aligned} \tag{A2}
$$

Polar flattening, quantified by ϵ, could be included by $n_z = n_z/\epsilon^2$ (Pilkington et al., 2015). The unit normal vector can be calculated from $\hat{n} = \vec{n}/|n|$.

The system of nonlinear equations defined by $F(\vec{x}) = \vec{0}$ is:

$$r_{MP} - r = 0 \tag{A3}$$

$$x_p - x - d\hat{n}_x = 0 \tag{A4}$$

$$y_p - y - d\hat{n}_y = 0 \tag{A5}$$

$$z_p - z - d\hat{n}_z = 0, \tag{A6}$$

where x_p, y_p, z_p are the KSM coordinates of the point of interest P (e.g., the spacecraft position), n_x, n_y, n_z are the outward directed components of the unit normal vector at position (x, y, z) on the MP, and d is the shortest distance along the normal vector between point P and the MP surface at (x, y, z).
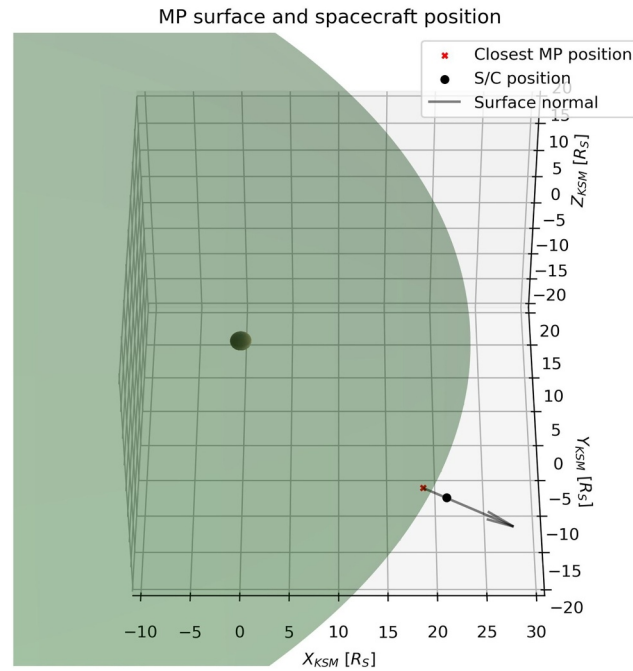
Figure A1. Schematic illustrating the shortest distance between a spacecraft position and an empirical MP surface constructed under solar wind pressure of D_p inferred from the observed boundary crossing. The arrow indicates the surface normal at the closest point to the spacecraft and that it passes directly through the spacecraft position; meaning that the red point is, indeed, the closest point.

This set of equations can be solved numerically using `fsolve` (Virtanen et al., 2020) which returns the roots $\vec{f}$ or the result of the last iteration if no roots were found. Here, the roots correspond to the coordinates (x, y, z) on the MP surface that is closest to the spacecraft position, and the magnitude of the shortest distance d as illustrated in Figure A1. Equation A3 constrains the (x, y, z) solution to lie on the MP surface, and Equations A4–A6 ensure that the closest point to the crossing is found.

The input to the function is a vector of arguments, starting with the initial guess of the roots $\vec{f} = (x_0, y_0, z_0, d)$, and returns values of the same length. Roots are successfully found when the set of Equations A3–A6 is satisfied. The final solution does not depend on the initial guess due to a unique solution that can satisfy these equations for any given spacecraft position and D_p of the MP surface. For simplicity, the starting guess was always set to the MP subsolar position and $d = 0$.

For the BS, the radial distance r_{BS} of the model surface is given by Went et al. (2011):

$$r_{BS}(x, y, z, \epsilon) = \frac{R_{SN}(1 + \epsilon)}{1 + \epsilon x/r}, \tag{A7}$$

where r_{SN} is the shock subsolar distance.

The normal vector for the BS surface is given by:

$$
\begin{aligned}
n_x &= \frac{x/r + \epsilon}{1 + \epsilon} \\
n_y &= \frac{y}{r(1 + \epsilon)} \\
n_z &= \frac{z}{r(1 + \epsilon)}
\end{aligned}
\tag{A8}
$$

An equivalent set of nonlinear equations as Equations A3–A6 can be produced for the BS boundary. The shortest distance between the BS surface and the spacecraft can be solved using the same technique as for the MP. Note that these distances would be negative inside the magnetosheath as the outward-pointing BS unit normal vectors would require a negative scaling to reach the spacecraft position.

Data Availability Statement

The list of bow shock and magnetopause boundary crossings is available at https://github.com/ikitcheng/BS_MP_Crossings_Cassini, where a detailed list of changes made may also be found. These were characterised by using the Cassini MAG and ELS data available from the Planetary Data System (https://pds.nasa.gov/).

References

Ala-Lahti, M. M., Kilpua, E. K. J., Dimmock, A. P., Osmane, A., Pulkkinen, T., & Souček, J. (2018). Statistical analysis of mirror mode waves in sheath regions driven by interplanetary coronal mass ejection. *Annales Geophysicae*, *36*(3), 793–808. https://doi.org/10.5194/angeo-36-793-2018

André, N., Erdös, G., & Dougherty, M. (2002). Overview of mirror mode fluctuations in the Jovian dusk magnetosheath: Cassini magnetometer observations. *Geophysical Research Letters*, *29*(20), 41–1–41–4. https://doi.org/10.1029/2002gl015187

Arridge, C. S., Achilleos, N., Dougherty, M. K., Khurana, K. K., & Russell, C. T. (2006). Modeling the size and shape of Saturn's magnetopause with variable dynamic pressure. *Journal of Geophysical Research*, *111*(A11), A11227. https://doi.org/10.1029/2005ja011574

Arridge, C. S., Gilbert, L. K., Lewis, G. R., Sittler, E. C., Jones, G. H., Kataria, D. O., et al. (2009). The effect of spacecraft radiation sources on electron moments from the Cassini CAPS electron spectrometer. *Planetary and Space Science*, *57*(7), 854–869. https://doi.org/10.1016/j.pss.2009.02.011

Balogh, A., Dougherty, M. K., Forsyth, R. J., Southwood, D. J., Smith, E. J., Tsurutani, B. T., et al. (1992). Magnetic field observations during the Ulysses flyby of Jupiter. *Science*, *257*(5076), 1515–1518. https://doi.org/10.1126/science.257.5076.1515

Bertucci, C., Mazelle, C., Crider, D., Mitchell, D., Sauer, K., Acuña, M., et al. (2004). MGS MAG/ER observations at the magnetic pileup boundary of mars: Draping enhancement and low frequency waves. *Advances in Space Research*, *33*(11), 1938–1944. https://doi.org/10.1016/j.asr.2003.04.054

Burne, S., Bertucci, C., Sergis, N., Morales, L. F., Achilleos, N., Sánchez-Cano, B., et al. (2023). Space weather in the Saturn–Titan system. *The Astrophysical Journal*, *948*(1), 37. https://doi.org/10.3847/1538-4357/acc738

Cattaneo, M. B. B., Basile, C., Moreno, G., & Richardson, J. D. (1998). Evolution of mirror structures in the magnetosheath of Saturn from the bow shock to the magnetopause. *Journal of Geophysical Research*, *103*(A6), 11961–11972. https://doi.org/10.1029/97ja03683

Cheng, I., Achilleos, N., Blanco-Cano, X., Bertucci, C., & Guio, P. (2024). Waves and instabilities in Saturn's magnetosheath: 2. Dispersion relation analysis. *Journal of Geophysical Research: Space Physics*.

Cheng, I., Achilleos, N., Masters, A., Lewis, G., Kane, M., & Guio, P. (2021). Electron bulk heating at Saturn's magnetopause. *Journal of Geophysical Research: Space Physics*, *126*(5), e2020JA028800. https://doi.org/10.1029/2020ja028800

Cheng, I., Achilleos, N., & Smith, A. (2022). Automated bow shock and magnetopause boundary detection with Cassini using threshold and deep learning methods. *Frontiers in Astronomy and Space Sciences*, *9*, 1016453. https://doi.org/10.3389/fspas.2022.1016453

Crooker, N. U., & Siscoe, G. L. (1977). A mechanism for pressure anisotropy and mirror instability in the dayside magnetosheath. *Journal of Geophysical Research*, *82*(1), 185–186. https://doi.org/10.1029/ja082i001p00185

Denton, R. E., Gary, S. P., Li, X., Anderson, B. J., LaBelle, J. W., & Lessard, M. (1995). Low-frequency fluctuations in the magnetosheath near the magnetopause. *Journal of Geophysical Research*, *100*(A4), 5665–5679. https://doi.org/10.1029/94ja03024

Dougherty, M. K., Kellock, S., Southwood, D. J., Balogh, A., Smith, E. J., Tsurutani, B. T., et al. (2004). The Cassini magnetic field investigation. *Space Science Reviews*, *114*(1–4), 331–383. https://doi.org/10.1007/s11214-004-1432-2

Enríquez-Rivera, O., Blanco-Cano, X., Russell, C. T., Jian, L. K., Luhmann, J. G., Simunac, K. D. C., et al. (2013). Mirror-mode storms inside stream interaction regions and in the ambient solar wind: A kinetic study. *Journal of Geophysical Research: Space Physics*, *118*(1), 17–28. https://doi.org/10.1029/2012ja018233

Erdős, G., & Balogh, A. (1996). Statistical properties of mirror mode structures observed by Ulysses in the magnetosheath of Jupiter. *Journal of Geophysical Research*, *101*(A1), 1–12. https://doi.org/10.1029/95ja02207

Gary, S. P. (1992). The mirror and ion cyclotron anisotropy instabilities. *Journal of Geophysical Research*, *97*(A6), 8519–8529. https://doi.org/10.1029/92ja00299

Génot, V., Schwartz, S. J., Mazelle, C., Balikhin, M., Dunlop, M., & Bauer, T. M. (2001). Kinetic study of the mirror mode. *Journal of Geophysical Research*, *106*(A10), 21611–21622. https://doi.org/10.1029/2000ja000457

Hadid, L. Z., Sahraoui, F., Kiyani, K. H., Retinò, A., Modolo, R., Canu, P., et al. (2015). Nature of the MHD and kinetic scale turbulence in the Magnetosheath of Saturn: Cassini observations. *The Astrophysical Journal*, *813*(2), L29. https://doi.org/10.1088/2041-8205/813/2/l29

Hasegawa, A. (1969). Drift mirror instability in the magnetosphere. *Physics of Fluids*, *12*(12), 2642–2650. https://doi.org/10.1063/1.1692407

Hau, L.-N., Chen, G.-W., & Chang, C.-K. (2020). Mirror mode waves immersed in magnetic reconnection. *The Astrophysical Journal Letters*, *903*(1), L12. https://doi.org/10.3847/2041-8213/abbf4a

Hubert, D. (1994). Nature and origin of wave modes in the dayside Earth magnetosheath. *Advances in Space Research*, *14*(7), 55–64. https://doi.org/10.1016/0273-1177(94)90048-5

Huddleston, D. E., Strangeway, R. J., Blanco-Cano, X., Russell, C. T., Kivelson, M. G., & Khurana, K. K. (1999). Mirror-mode structures at the Galileo-Io flyby: Instability criterion and dispersion analysis. *Journal of Geophysical Research*, *104*(A8), 17479–17489. https://doi.org/10.1029/1999ja900195

Joy, S. P., Kivelson, M. G., Walker, R. J., Khurana, K. K., Russell, C. T., & Paterson, W. R. (2006). Mirror mode structures in the Jovian magnetosheath. *Journal of Geophysical Research*, *111*(A12), A12212. https://doi.org/10.1029/2006ja011985

Krauss-Varban, D., Omidi, N., & Quest, K. B. (1994). Mode properties of low-frequency waves: Kinetic theory versus hall-MHD. *Journal of Geophysical Research*, *99*(A4), 5987–6009. https://doi.org/10.1029/93JA03202

Krimigis, S. M., Mitchell, D. G., Hamilton, D. C., Livi, S., Dandouras, J., Jaskulek, S., et al. (2004). Magnetosphere Imaging Instrument (MIMI) on the Cassini mission to Saturn/Titan. *Space Science Reviews*, *114*(1–4), 233–329. https://doi.org/10.1007/s11214-004-1410-8

Lacombe, C., & Belmont, G. (1995). Waves in the Earth's magnetosheath: Observations and interpretations. *Advances in Space Research*, *15*(8–9), 329–340. https://doi.org/10.1016/0273-1177(94)00113-f

Lewis, G. R., André, N., Arridge, C. S., Coates, A. J., Gilbert, L. K., Linder, D. R., et al. (2008). Derivation of density and temperature from the Cassini-Huygens CAPS electron spectrometer. *Planetary and Space Science*, *56*(7), 901–912. https://doi.org/10.1016/j.pss.2007.12.017

Liou, K., Paranicas, C., Vines, S., Kollmann, P., Allen, R. C., Clark, G. B., et al. (2021). Dawn-Dusk asymmetry in energetic (>20 keV) particles adjacent to Saturn's magnetopause. *Journal of Geophysical Research: Space Physics*, *126*(2), e2020JA028264. https://doi.org/10.1029/2020ja028264

Masters, A., Eastwood, J. P., Swisdak, M., Thomsen, M. F., Russell, C. T., Sergis, N., et al. (2012). The importance of plasma β conditions for magnetic reconnection at Saturn's magnetopause. *Geophysical Research Letters*, *39*(8), 1–6. https://doi.org/10.1029/2012GL051372

Mauk, B. H., Mitchell, D. G., McEntire, R. W., Paranicas, C. P., Roelof, E. C., Williams, D. J., et al. (2004). Energetic ion characteristics and neutral gas interactions in Jupiter's magnetosphere. *Journal of Geophysical Research*, *109*(A9), A09S12. https://doi.org/10.1029/2003JA010270

Meeks, Z., & Simon, S. (2017). Magnetic signatures of ion cyclotron waves during Cassini's high-inclination orbits of Saturn. *Planetary and Space Science*, *136*, 34–45. https://doi.org/10.1016/j.pss.2016.12.006

Nykyri, K., Chu, C., Ma, X., Fuselier, S. A., & Rice, R. (2019). First MMS observation of energetic particles trapped in high-latitude magnetic field depressions. *Journal of Geophysical Research: Space Physics*, *124*(1), 197–210. https://doi.org/10.1029/2018ja026131

Pilkington, N. M., Achilleos, N., Arridge, C. S., Guio, P., Masters, A., Ray, L. C., et al. (2015). Internally driven large-scale changes in the size of Saturn's magnetosphere. *Journal of Geophysical Research A: Space Physics*, *120*(9), 7289–7306. https://doi.org/10.1002/2015JA021290

Russell, C. T., Blanco-Cano, X., Jian, L. K., & Luhmann, J. G. (2009). Mirror-mode storms: STEREO observations of protracted generation of small amplitude waves. *Geophysical Research Letters*, *36*(5), L05106. https://doi.org/10.1029/2008gl037113

Russell, C. T., Jian, L. K., Luhmann, J. G., Zhang, T. L., Neubauer, F. M., Skoug, R. M., et al. (2008). Mirror mode waves: Messengers from the coronal heating region. *Geophysical Research Letters*, *35*(15), L15101. https://doi.org/10.1029/2008gl034096

Russell, C. T., Kivelson, M. G., Khurana, K. K., & Huddleston, D. E. (1998). Magnetic fluctuations close to IO: Ion cyclotron and mirror mode wave properties. *Planetary and Space Science*, *47*(1–2), 143–150. https://doi.org/10.1016/s0032-0633(98)00090-7

Russell, C. T., Leisner, J. S., Arridge, C. S., Dougherty, M. K., & Blanco-Cano, X. (2006). Nature of magnetic fluctuations in Saturn's middle magnetosphere. *Journal of Geophysical Research*, *111*(A12), A12205. https://doi.org/10.1029/2006ja011921

Russell, C. T., Riedler, W., Schwingenschuh, K., & Yeroshenko, Y. (1987). Mirror instability in the magnetosphere of comet Halley. *Geophysical Research Letters*, *14*(6), 644–647. https://doi.org/10.1029/gl014i006p00644

Russell, C. T., Song, P., & Lepping, R. P. (1989). The Uranian magnetopause: Lessons from Earth. *Geophysical Research Letters*, *16*(12), 1485–1488. https://doi.org/10.1029/gl016i012p01485

Schmid, D., Plaschke, F., Narita, Y., Heyner, D., Mieth, J. Z. D., Anderson, B. J., et al. (2020). Magnetometer in-flight offset accuracy for the BepiColombo spacecraft. *Annales Geophysicae*, *38*(4), 823–832. https://doi.org/10.5194/angeo-38-823-2020

Schwartz, S. J., Burgess, D., & Moses, J. J. (1996). Low-frequency waves in the Earth's magnetosheath: Present status. *Annales Geophysicae*, *14*(11), 1134–1150. https://doi.org/10.1007/s00585-996-1134-z

Sergis, N., Jackman, C. M., Masters, A., Krimigis, S. M., Thomsen, M. F., Hamilton, D. C., et al. (2013). Particle and magnetic field properties of the Saturnian magnetosheath: Presence and upstream escape of hot magnetospheric plasma. *Journal of Geophysical Research: Space Physics*, *118*(4), 1620–1634. https://doi.org/10.1002/jgra.50164

Slavin, J. A., Smith, E. J., Gazis, P. R., & Mihalov, J. D. (1983). A pioneer-voyager study of the solar wind interaction with Saturn. *Geophysical Research Letters*, *10*(1), 9–12. https://doi.org/10.1029/gl010i001p00009

Soto-Chavez, A. R., Lanzerotti, L. J., Manweiler, J. W., Gerrard, A., Cohen, R., Xia, Z., et al. (2019). Observational evidence of the drift-mirror plasma instability in Earth's inner magnetosphere. *Physics of Plasmas*, *26*(4), 042110. https://doi.org/10.1063/1.5083629

Soucek, J., Escoubet, C. P., & Grison, B. (2015). Magnetosheath plasma stability and ULF wave occurrence as a function of location in the magnetosheath and upstream bow shock parameters. *Journal of Geophysical Research: Space Physics*, *120*(4), 2838–2850. https://doi.org/10.1002/2015ja021087

Soucek, J., Lucek, E., & Dandouras, I. (2008). Properties of magnetosheath mirror modes observed by cluster and their response to changes in plasma parameters. *Journal of Geophysical Research*, *113*(A4), A04203. https://doi.org/10.1029/2007ja012649

Southwood, D. J., & Kivelson, M. G. (1993). Mirror instability: 1. Physical mechanism of linear instability. *Journal of Geophysical Research*, *98*(A6), 9181–9187. https://doi.org/10.1029/92ja02837

Sulaiman, A. H., Jia, X., Achilleos, N., Sergis, N., Gurnett, D. A., & Kurth, W. S. (2017). Large-scale solar wind flow around Saturn's non-axisymmetric magnetosphere. *Journal of Geophysical Research: Space Physics*, *122*(9), 9198–9206. https://doi.org/10.1002/2017ja024595

Sulaiman, A. H., Masters, A., & Dougherty, M. K. (2016). Characterization of Saturn's bow shock: Magnetic field observations of quasi-perpendicular shocks. *Journal of Geophysical Research: Space Physics*, *121*(5), 4425–4434. https://doi.org/10.1002/2016ja022449

Swisdak, M., Opher, M., Drake, J. F., & Alouani Bibi, F. (2010). The vector direction of the interstellar magnetic field outside the heliosphere. *Astrophysical Journal*, *710*(2), 1769–1775. https://doi.org/10.1088/0004-637X/710/2/1769

Swisdak, M., Rogers, B. N., Drake, J. F., & Shay, M. A. (2003). Diamagnetic suppression of component magnetic reconnection at the magnetopause. *Journal of Geophysical Research*, *108*(A5), 1218. https://doi.org/10.1029/2002JA009726

Thomsen, M. F., Reisenfeld, D. B., Delapp, D. M., Tokar, R. L., Young, D. T., Crary, F. J., et al. (2010). Survey of ion plasma parameters in Saturn's magnetosphere. *Journal of Geophysical Research*, *115*(10), 1–22. https://doi.org/10.1029/2010JA015267

Tsurutani, B. T., Lakhina, G. S., Verkhoglyadova, O. P., Echer, E., Guarnieri, F. L., Narita, Y., et al. (2011). Magnetosheath and Heliosheath mirror mode structures, interplanetary magnetic decreases, and linear magnetic decreases: Differences and distinguishing features. *Journal of Geophysical Research*, *116*(A2), A02103. https://doi.org/10.1029/2010ja015913

Tsurutani, B. T., Richardson, I. G., Lepping, R. P., Zwickl, R. D., Jones, D. E., Smith, E. J., et al. (1984). Drift mirror mode waves in the distant (x $\simeq$ 200 R_e) magnetosheath. *Geophysical Research Letters*, *11*(10), 1102–1105. https://doi.org/10.1029/gl011i010p01102

Tsurutani, B. T., Smith, E. J., Anderson, R. R., Ogilvie, K. W., Scudder, J. D., Baker, D. N., et al. (1982). Lion roars and nonoscillatory drift mirror waves in the magnetosheath. *Journal of Geophysical Research*, *87*(A8), 6060–6072. https://doi.org/10.1029/ja087ia08p06060

Tsurutani, B. T., Southwood, D. J., Smith, E. J., & Balogh, A. (1992). Nonlinear magnetosonic waves and mirror mode structures in the March 1991 Ulysses interplanetary event. *Geophysical Research Letters*, *19*(12), 1267–1270. https://doi.org/10.1029/92gl00782

Tsurutani, B. T., Southwood, D. J., Smith, E. J., & Balogh, A. (1993). A survey of low frequency waves at Jupiter: The Ulysses encounter. *Journal of Geophysical Research*, *98*(A12), 21203–21216. https://doi.org/10.1029/93ja02586

Violante, L., Cattaneo, M. B. B., Moreno, G., & Richardson, J. D. (1995). Observations of mirror waves and plasma depletion layer upstream of Saturn's magnetopause. *Journal of Geophysical Research*, *100*(A7), 12047–12055. https://doi.org/10.1029/94ja02703

Virtanen, P., Gommers, R., Oliphant, T. E., Haberland, M., Reddy, T., Cournapeau, D., et al. (2020). SciPy 1.0: Fundamental algorithms for scientific computing in Python. *Nature Methods*, *17*(3), 261–272. https://doi.org/10.1038/s41592-019-0686-2

Volwerk, M., Simon Wedlund, C., Mautner, D., Rojas Mata, S., Stenberg Wieser, G., Futaana, Y., et al. (2022). Statistical distribution of mirror mode-like structures in the magnetosheaths of unmagnetised planets: 2. Venus as observed by the Venus express spacecraft. *EGUsphere*, *2022*, 1–30. https://doi.org/10.5194/egusphere-2022-645

Wedlund, C. S., Volwerk, M., Mazelle, C., Mata, S. R., Wieser, G. S., Futaana, Y., et al. (2023). Statistical distribution of mirror-mode-like structures in the magnetosheaths of unmagnetised planets – Part 1: Mars as observed by the MAVEN spacecraft. *Annales Geophysicae*, *41*(1), 225–251. https://doi.org/10.5194/angeo-41-225-2023

Went, D. R., Hospodarsky, G. B., Masters, A., Hansen, K. C., & Dougherty, M. K. (2011). A new semiempirical model of Saturn's bow shock based on propagated solar wind parameters. *Journal of Geophysical Research*, *116*(7), 1–9. https://doi.org/10.1029/2010JA016349

Winterhalter, D., Neugebauer, M., Goldstein, B. E., Smith, E. J., Bame, S. J., & Balogh, A. (1994). Ulysses field and plasma observations of magnetic holes in the solar wind and their relation to mirror-mode structures. *Journal of Geophysical Research*, *99*(A12), 23371–23381. https://doi.org/10.1029/94ja01977

Young, D. T., Berthelier, J. J., Blanc, M., Burch, J. L., Coates, A. J., Goldstein, R., et al. (2004). Cassini plasma spectrometer investigation. *Space Science Reviews*, *114*(1–4), 1–112. https://doi.org/10.1007/s11214-004-1406-4

Zhang, T. L., Russell, C. T., Baumjohann, W., Jian, L. K., Balikhin, M. A., Cao, J. B., et al. (2008). Characteristic size and shape of the mirror mode structures in the solar wind at 0.72 AU. *Geophysical Research Letters*, *35*(10), L10106. https://doi.org/10.1029/2008gl033793

Zhao, J., Wang, T., Shi, C., Graham, D. B., Dunlop, M. W., He, J., et al. (2019). Ion and electron dynamics in the presence of mirror, electromagnetic ion cyclotron, and whistler waves. *The Astrophysical Journal*, *883*(2), 185. https://doi.org/10.3847/1538-4357/ab3bd1

Zhong, Z. H., Zhou, M., Liu, Y.-H., Deng, X. H., Tang, R. X., Graham, D. B., et al. (2022). Stacked electron diffusion regions and electron Kelvin–Helmholtz vortices within the ion diffusion region of collisionless magnetic reconnection. *The Astrophysical Journal Letters*, *926*(2), L27. https://doi.org/10.3847/2041-8213/ac4dee